Monthly Notices
of the
ROYAL ASTRONOMICAL SOCIETY

MNRAS **497,** 2455–2468 (2020)
Advance Access publication 2020 July 9

doi:10.1093/mnras/staa1990

Gamma-ray counterparts of 2WHSP high-synchrotron-peaked BL Lac objects as possible signatures of ultra-high-energy cosmic ray emission

Michael W. Toomey [1,2,3,4]★ Foteini Oikonomou [3,5,6,7] and Kohta Murase[3,4,8]

[1]*Brown Theoretical Physics Center, Brown University, Providence, RI 02912, USA*
[2]*Department of Physics, Brown University, Providence, RI 02912, USA*
[3]*Department of Physics, The Pennsylvania State University, University Park, PA 16802, USA*
[4]*Department of Astronomy and Astrophysics, The Pennsylvania State University, University Park, PA 16802, USA*
[5]*Physik-Department, Technische Universität München, James-Frank-Str. 1, D-85748 Garching bei München, Germany*
[6]*European Southern Observatory, Karl-Schwarzschild-Str. 2, D-85748 Garching bei Munchen, Germany*
[7]*Institutt for fysikk, NTNU, Trondheim, 7491 Norway*
[8]*Yukawa Institute for Theoretical Physics, Kyoto University, Kyoto 606-8502, Japan*

Accepted 2020 June 29. Received 2020 June 23; in original form 2020 March 4

ABSTRACT

We present a search for high-energy γ-ray emission from 566 Active Galactic Nuclei at redshift $z > 0.2$, from the 2WHSP catalogue of high-synchrotron peaked BL Lac objects with 8 yr of *Fermi*-LAT data. We focus on a redshift range where electromagnetic cascade emission induced by ultra-high-energy cosmic rays can be distinguished from leptonic emission based on the spectral properties of the sources. Our analysis leads to the detection of 160 sources above $\approx 5\sigma$ (TS $\geq$25) in the 1–300 GeV energy range. By discriminating significant sources based on their γ-ray fluxes, variability properties, and photon index in the *Fermi*-LAT energy range, and modelling the expected hadronic signal in the TeV regime, we select a list of promising sources as potential candidate ultra-high-energy cosmic ray emitters for follow-up observations by Imaging Atmospheric Cherenkov Telescopes.

Key words: galaxies: active – galaxies: high-redshift – gamma rays: galaxies.

1 INTRODUCTION

The *Fermi* Gamma-ray Space Telescope (Atwood et al. 2009) and Imaging Atmospheric Cherenkov Telescopes (IACTs) have dramatically increased the number of known γ-ray sources, as well as our knowledge of the non-thermal Universe. Among the observed extragalactic γ-ray sources, blazars, active galactic nuclei (AGNs) with jets aligned with the observer's line of sight (e.g. Urry & Padovani 1995), are by far the most numerous. They exhibit superluminal motion, and are some of the most powerful steady sources in the Universe. Additionally, they dominate the γ-ray sky and play an important role in the energy budget of the Universe (Murase & Fukugita 2019).

Categorized as either BL Lacertae (BL Lac) objects or Flat Spectrum Radio Quasars (FSRQs), based on the properties of their optical spectra, blazars are among the brightest objects in the Universe. Blazars possess spectral energy distributions (SEDs) with a characteristic double hump shape. The lower energy peak is generally thought to be powered by the synchrotron emission of electrons in the blazar jet. The origin of the high-energy peak is a subject of debate. In conventional leptonic scenarios, the γ-ray emission is assumed to be powered by inverse Compton radiation (Maraschi, Ghisellini & Celotti 1992; Sikora, Begelman & Rees 1994), but it could also have a hadronic origin (Aharonian 2000; Mücke & Protheroe 2001). BL Lac objects are further sub-classified according to the value of the frequency (in the source rest-frame) at which the synchrotron peak of the SED occurs. Low-energy ($\nu_S < 10^{14}$ Hz), intermediate-energy ($10^{14} < \nu_S < 10^{15}$ Hz) and high-energy ($\nu_S > 10^{15}$ Hz) synchrotron peaked, referred to in short as LSP, ISP, and HSP respectively (Padovani & Giommi 1995; Fermi-LAT Collaboration 2010).

More recently, observations with IACTs have revealed an additional class of BL Lac objects, whose spectrum in the *Fermi*-LAT energy range is hard (meaning that the spectral index in this energy range $\gamma < 2$), placing their peak of the high-energy 'hump' in the SED, after accounting for absorption during their extragalactic propagation, in the TeV energy range. Additionally, these sources typically possess $\nu_S > 10^{17}$ Hz. These properties are suggestive of extreme particle acceleration which has led to them being referred to as extreme HSPs (Costamante et al. 2001, 2018; Biteau et al. 2020).

One of the greatest mysteries in particle astrophysics today is the origin of ultra-high-energy cosmic-rays (UHECRs). Such particles are observed with energies in excess of $\approx 10^{20}$ eV (see e.g. reviews by Kotera & Olinto 2011; Mollerach & Roulet 2018; Alves Batista et al. 2019; Anchordoqui 2019). Since the Larmor radius for cosmic-rays above the *ankle*, at $\sim 4 \times 10^{18}$ eV, exceeds that of the Galaxy, these UHECRs are very likely of extragalactic origin. One of the most promising candidates proposed as the sources of UHECRs are AGNs (Ginzburg & Syrovatskii 1964; Hillas 1984). Blazars, specifically, have often been proposed as sites of UHECR acceleration (see e.g. Dermer & Razzaque 2010; Murase et al. 2012b; Rodrigues et al. 2018, and references therein).

★ E-mail: michael_toomey@brown.edu

This is particularly true for extreme HSP BL Lac objects. Attempts to describe the origin of their hard TeV spectra with standard leptonic models often require extreme parameters (e.g. Katarzynski et al. 2006). An alternative scenario for the observed γ-ray emission of extreme HSPs is that it is secondary emission from UHECRs (e.g. Essey & Kusenko 2010; Essey et al. 2011; Murase et al. 2012b; Aharonian et al. 2013; Takami, Murase & Dermer 2013; Oikonomou, Murase & Kotera 2014; Takami, Murase & Dermer 2016; Tavecchio et al. 2019). If these sources produce UHECRs, these will interact with photons from the extragalactic background light (EBL) and the cosmic microwave background (CMB), and produce electron–positron pairs (Bethe-Heitler) emission, and pionic γ-rays. However, the spectrum of UHECR-induced secondary γ-rays is expected to extend to higher energies than in standard leptonic scenarios due to the continuous injection of high-energy leptons via the Bethe-Heitler (BH) pair-production process during intergalactic propagation, leading to a natural explanation for the observed hard TeV spectra.

Primary and secondary γ-rays with energy $E_\gamma \sim (m_e^2c^4)/\varepsilon_\gamma \sim 260\,(1\,\mathrm{eV}/\varepsilon_\gamma)\,\mathrm{GeV}$, interact with photons of the EBL and the CMB with energy ε_γ, which results in the production of electron–positron pairs (Gould & Schréder 1966; Stecker, de Jager & Salamon 1992). Electrons and positrons produced in interactions of γ-rays with the EBL/CMB inverse Compton upscatter background photons, and generate secondary γ-rays. The two processes (pair-production and inverse Compton emission) produce an electromagnetic 'cascade' in the intergalactic medium, until the γ-rays drop below the threshold for pair production on the EBL. During the intergalactic propagation of the cascade emission, the electrons (and positrons) get deflected in the presence of intergalactic magnetic fields (IGMFs), causing either magnetic broadening of the cascade emission, or, in the presence of a stronger field, a suppression of the observed GeV cascade flux from the source (Gould & Rephaeli 1978; Aharonian, Coppi & Volk 1994). The detection (or absence of) the cascade emission from TeV emitting blazars can result in the measurement of (or lower bound on) the IGMF in the line of sight from these sources. Similarly the detection of magnetic broadening, 'halo' emission, can result in a measurement of the strength of IGMFs (e.g. Elyiv, Neronov & Semikoz 2009; Neronov & Semikoz 2009; H. E. S. S. Collaboration 2014; Archambault et al. 2017). High-redshift, hard-spectrum blazars, whose intrinsic spectrum extends beyond TeV energies are thus ideal sources to look for the signatures of the effects of the IGMF (cascade flux, and halo component), as the cascade emission in the GeV spectrum dominates the observed emission in this energy band. This combination of parameters maximizes the expected cascade emission in these sources, and in the case of non-observation of the expected cascade emission, can result in lower limits on the IGMF strength. For the same reason, the expected halo component is maximal for high-redshift, hard-spectrum sources (although at the disadvantage of having an overall fainter source). The highest redshift blazars that have been detected to date with IACTs are PKS 1441+25 (Abeysekara et al. 2015) and S3 0218+35 (Ahnen et al. 2016). These are of the FSRQ type, and were detected up to ~200 GeV energy. They are thus not expected to exhibit the signature of UHECR emission which has been proposed for extreme HSPs in their γ-ray spectra, but demonstrate the possible reach of future, deeper, IACT observations.

1.1 Time variability

An important observational distinction between leptonic and UHECR-induced intergalactic cascade emissions is related to the different deflections experienced by the leptonic and UHECR beam in the IGMF. As a result, one expects different variability properties of the γ-ray emission in these two cases. In the case of a leptonic beam, time delays are only relevant for the secondary (cascade) emission, and come from the deflections of the electrons produced in the interactions of the primary γ-rays with background photons. Electrons with energy E'_e (in the cosmic rest frame at redshift z), and Lorentz factor $\gamma'_e = E'_e/(m_ec^2)$, traversing a region with magnetic field strength B, have a Larmor radius $r_\mathrm{L} \approx eB/E'_e$, where e is the charge of the electron. Such electrons will experience deflections of order $\theta_\mathrm{IC} \approx \sqrt{2/3}(\lambda_\mathrm{IC}/r_\mathrm{L})$ before inverse Compton upscattering CMB photons, after, on average, one inverse Compton cooling length $\lambda_\mathrm{IC} = 3m_ec^2/(4\sigma_T U_\mathrm{CMB}\gamma'_e) \approx 70\,\mathrm{kpc}\,(E'_e/5\,\mathrm{TeV})^{-1}(1+z)^{-4}$, where σ_T is the Thompson cross-section and $U_\mathrm{CMB} \simeq 0.26\,\mathrm{eV}\,(1+z)^4$ is the energy density of the CMB at redshift z.

The typical time delay experienced by cascade photons due to the deflections of the electrons is of order, (e.g. Murase et al. 2008; Takahashi et al. 2008; Dermer et al. 2011), $\Delta t_\mathrm{IC,IGMF}/(1+z) \approx \theta^2_\mathrm{IC}(\lambda_\mathrm{IC}+\lambda_{\gamma\gamma})/2c$. Here, $\lambda_{\gamma\gamma} \sim 20\,\mathrm{Mpc}\,(n_\mathrm{EBL}/0.1\,\mathrm{cm}^3)^{-1}$ is the average distance travelled by a primary γ-ray before it interacts with an EBL photon to create an electron–positron pair. In the above expression, n_EBL is the number density of EBL photons, normalized to the value relevant for interactions with 10 TeV γ-rays. The electrons subsequently upscatter CMB photons via the inverse-Compton process, typically to energy $E_\gamma \approx (4/3)\gamma'^2_e\varepsilon_\mathrm{CMB}$, where $\varepsilon_\mathrm{CMB} \approx 2.8k_BT_\mathrm{CMB,0}$ and k_B the Boltzmann constant, and $T_\mathrm{0,CMB}$ the temperature of the CMB at $z=0$. For such γ-rays with energy E_γ from a source at $z \ll 1$, we obtain a characteristic time delay (e.g. Murase, Mészáros & Zhang 2009),

$$\frac{\Delta t_\mathrm{IC,IGMF}}{(1+z)} \approx \frac{\theta^2_\mathrm{IC}}{2c}(\lambda_\mathrm{IC}+\lambda_{\gamma\gamma}) \sim 4\times10^5\,\mathrm{yr}\left(\frac{E_\gamma}{0.1\,\mathrm{TeV}}\right)^{-2} \times \left(\frac{B}{10^{-14}\,\mathrm{G}}\right)^2\left(\frac{\lambda_{\gamma\gamma}}{20\,\mathrm{Mpc}}\right). \quad (1)$$

Thus, any detectable variable emission in short time-scales is likely primary in origin. An additional, slowly variable component may exist, due to the reprocessed emission, if the IGMF is sufficiently low ($B \lesssim 10^{-17}$ G).

In the UHECR-induced intergalactic cascade scenario, there is no primary γ-ray component. The main energy loss channel for protons with energy less than 10^{19} eV is through the Bethe–Heitler pair-production process. The trajectory of the protons may be regarded as a random walk through individual scattering centres of size, $l_c \sim \mathcal{O}(\mathrm{Mpc})$. The Larmor radius of an UHECR with energy E_p is, $r_{\mathrm{L},p} \sim eB/E_p \sim 800\,\mathrm{Mpc}(B/10^{17}\,\mathrm{G})(E_p/10^{17}\,\mathrm{eV})^{-1}$. After crossing a scattering centre of size l_c the proton experiences a deflection of order $\theta_p \approx \sqrt{2/3}l_c/r_{\mathrm{L},p}$ and a time delay of order $\Delta t_0 \sim (l_c/c)\theta_p^2$. Thus, the total time delay experienced after travelling the characteristic energy loss length of the Bethe–Heitler process, λ_BH, is of order, $\Delta t_p \sim (\lambda_\mathrm{BH}/l_c)\Delta t_0 \sim (\lambda_\mathrm{BH}/c)\theta_p^2 \sim 20\,\mathrm{yr}\,(E_p/10^{17}\,\mathrm{eV})(B/10^{-14}\,\mathrm{G})^2(\lambda_\mathrm{BH}/1\,\mathrm{Gpc})(1+z)$ (Murase et al. 2012b; Prosekin et al. 2012). At every interaction the proton produces electrons (and positrons) which cascade down to GeV energies over a length scale of order λ_IC. Thus, in this case, the relevant time delay is $\max(\Delta t_\mathrm{IC,IGMF}, \Delta t_p)$, i.e. the maximum of the delays experienced by the protons and those of the leptonic cascade emission given by equation (1). As a result, we expect that the sources whose emission is dominated by UHECR cascades should be non-variable or at most slowly variable.

The search for variability is a strong motivation for this work. However, though the absence or weakness of the variability is one

of the crucial signatures of the UHECR-induced cascade scenario, negative detection itself is not proof for the UHECR origin of the emission. This is because, even if the variability is present, it may simply be below the experimental sensitivity.

Our goal is to identify sources which have a hard spectrum in the GeV energy range. Such sources are good candidates for very high-energy (VHE) follow-up observations, which can reveal TeV spectra of extreme HSP blazars, and possibly the signatures of UHECR acceleration and information on IGMFs. Additionally, we investigate variability properties of our source sample. The presence of the variability can rule out hadronic origin of the γ-ray emission. The non-detection of variability is harder to interpret in this context, as it can be caused by either intergalactic propagation effects or insufficient sensitivities of the instruments. Nevertheless, we make inferences by examining the entire sample, and trends as a function of redshift and γ-ray flux.

The layout of the paper is as follows. In Section 2 we discuss the selection of our catalogue and the analysis of *Fermi*-LAT data, including the calculation of the time variability. In Section 3 we discuss our modelling of the leptonic and hadronic emissions in the TeV regime. In Section 4 we present the results of our work and in Section 5 we discuss our results and propose avenues for further study.

2 ANALYSIS

2.1 Data selection

For our analysis we opt to use the 2WHSP catalogue of HSP blazars (Chang et al. 2017), which was, until recently, the most complete catalogue of HSP and candidate extreme-HSP sources (see discussion in Section 5). All sources from the catalogue with redshifts $\geq$0.2 were selected and submitted to a full *Fermi* analysis, a total of 566 sources. This was the only cut made on the 2WHSP catalogue, motivated by the theoretical prediction that UHECR-induced cascade emission can be more prominent for higher redshift HSPs (Murase et al. 2012b; Takami et al. 2013). Note that some sources in the catalogue only have a redshift with a lower limit. We still include these in the analysis but interpret results differently where relevant.

This sample of high redshift blazars from the 2WHSP catalogue forms the basis of the sources studied in this analysis. An analysis searching for γ-ray emission was conducted by the authors of the 1BIGB catalogue (Arsioli & Chang 2017) (see also Arsioli et al. 2018). However, these analyses did not include a study of source variability. In order to determine potential cosmic-ray accelerators based on VHE γ-rays, this information can be critical. In Section 4 we elaborate further on how our results compare to and differ from those of Arsioli & Chang (2017).

Many of the sources studied in this analysis have a counterpart in the 3FGL (Acero et al. 2015) and the recently released 4FGL catalogue (The Fermi-LAT collaboration 2019). However, the variability analysis from the 4FGL, or the previous 3FGL, is not appropriate for our work due to the inclusion of sub-GeV photons. In the UHECR-induced cascade scenario, cascade emission is expected to be dominant in the 10–100 GeV range as we show in the following sections. At the sub-GeV energy range, because of the IGMF suppression of the cascade component, primary photons that are intrinsically variable would dominate the spectrum for blazars. However, we would not have sufficient statistics for the variability analysis if we focused on the high-energy data in the 30–100 GeV range only. Therefore in this work we have chosen the 1–100 GeV energy range for our analysis. This is not ideal but still useful to see the variability and discriminate between the leptonic and hadronic scenarios. We further note that since the sources of interest in our study have a hard spectrum in the *Fermi* energy range, it would be more challenging to detect the variability in the 100 MeV–1 GeV energy range than for the average of 4FGL sources.

2.2 Data analysis

An unbinned maximum-likelihood approach was used in this work for spectral analysis utilizing *Fermi* Science Tools v10r0p5. For each blazar candidate, a region of interest 8° in radius was created from Pass 8 SOURCE class (*evclass* = 128) photons that where detected on both the FRONT and BACK of the LAT detectors (*evtype* = 3). Data were filtered temporally from 2008 August 5 (239587201 MET) to 2016 September 24 (496426332 MET) culminating in a total of 8.2 yr of data. Data were additionally filtered by considering photons of energies 1.0–300 GeV and setting a maximum zenith angle of 100° to avoid atmospheric background. Periods where data taken from LAT were of poor quality were removed utilizing the tool *gtmktime*. At this step, the LAT team's recommended filter expression for SOURCE class photons (DATA_QUAL>0)&&(LAT_CONFIG==1) was used.

For each source an exposure hypercube was calculated – a measure of the amount of time a position on the sky has spent at a certain inclination angle. The exposure hypercube was computed with *gtltcube* by binning the off-axis angle in increments of 0.025 $\cos\theta_{\rm OA}$ and setting the spatial grid size to 1°. For our analysis, we follow the *Fermi*-LAT recommendation to implement the zenith angle cut for exposure during the calculation of the exposure hypercube as opposed to during the determination of good time intervals with *gtmktime*. The exposure map was then calculated for a region 18° in radius, with 72 latitudinal and longitudinal points, and 24 logarithmically uniform energy bins.

We conducted a sanity check of our own implementation of *Fermi* Tools used in this analysis by utilizing the FERMIPY package (Wood et al. 2017). The results obtained with the two methods were found to be consistent. We did not use the FERMIPY package for our results as an unbinned analysis method was not available.

2.3 Modelling

For each candidate γ-ray blazar, a model was constructed using known 3FGL sources, the Galactic diffuse emission model *gll_iem_v06*, and isotropic diffuse model *iso_P8R2_SOURCE_V6_v06* with *make3FGLxml*. Non-3FGL sources were added to the model as a simple power law,

$$\frac{{\rm d}N}{{\rm d}E} = N_0 \left[\frac{E}{E_0}\right]^{-\gamma}. \quad (2)$$

The photon index, γ, and normalizations, N_0, were set free to be fit but the pivot energy, E_0, was fixed at 3.0 GeV for non-3FGL sources and set to 3FGL catalogue values otherwise. The normalizations of the Galactic and isotropic diffuse emissions were fit, in addition to the normalization of all sources within 3° and variable sources out to 5°. The maximum likelihood for each source was then computed using an unbinned technique with the *NEWMINUIT* minimizer implemented by the *UnbinnedAnalysis* module from *Fermi* Tools.

2.4 Time variability

A detailed variability analysis was conducted for significant sources – those above a *TS* of 25. Variability was determined by analysing the sources at 60 d intervals with two different models. The first

Table 1. Results from the analysis of 2WHSP sources. Included is the name from the 2WHSP catalogue, whether it is a Class I or II source, the luminosity from 1–300 GeV, L_{44}, in units of 10^{44} erg s^{-1}, the 1–300 GeV photon flux, $(\mathrm{d}N/\mathrm{d}t)_{-10}$, in units of 10^{-10} cm^{-2} s^{-1}, the test statistic from the likelihood fit, TS, the normalization and its error scaled by 10^{-11} cm^{-2} s^{-1} GeV^{-1}, N_{-11} and σ_N, the photon index γ and its error σ_γ, the variability index TS_V (> 63.17 is a variable source), the source redshift z, alternative identifier, and the logarithm of the synchrotron peak frequency, $\log \nu_{\mathrm{S,pk}}$ in units of log Hz. The latter three entries are obtained from the 2WHSP catalogue. Listed here are the results based on our source selection criteria. The full table, with all sources from the analysis, is available in the Appendix.

2WHSP name	Class	L_{44}	$(\frac{\mathrm{d}N}{\mathrm{d}t})_{-10}$	TS	N_{-11}	σ_N	γ	σ_γ	TS_V	z	Other name	$\log \nu_{\mathrm{S,pk}}$
J011904.6-145858	II	45.54	2.82	134.42	1.82	0.29	1.77	0.12	27.0	>0.530	3FGL J0118.9-1457	16.1
J050657.7-543503	I	25.07	5.05	488.2	2.21	0.21	1.56	0.07	40.6	>0.260	RBS 621	16.2
J060408.5-481725	II	20.5	2.69	132.76	0.26	0.05	1.73	0.11	37.1	>0.370	1ES 0602-482	16.2
J101244.2+422957		19.77	2.78	157.36	1.01	0.14	1.74	0.11	29.3	0.365	3FGL J1012.7+4229	16.8
J103118.4+505335	I	41.89	9.22	1014.9	7.26	0.48	1.74	0.05	52.7	0.360	1ES 1028+511	17.0
J112453.8+493409	II	93.35	4.89	362.65	2.91	0.29	1.78	0.08	63.9	>0.570	RBS 981	16.5
J124312.7+362743	II	99.06	21.98	2594.8	33.10	1.52	1.78	0.03	62.1	1.065	Ton 116	16.2
J141756.5+254324	I	10.14	2.86	147.3	7.2	1.65	1.63	0.08	24.6	0.237	RBS 1366	17.4
J143657.7+563924	II	57.3	5.79	522.39	8.28	0.8	1.77	0.06	47.4	>0.430	RBS 1409	16.9
J150340.6-154113	I	65.09	9.18	439.69	5.04	0.42	1.79	0.07	52.0	>0.380	RBS 1457	17.6
J175615.9+552218	II	45.88	3.68	223.86	3.85	0.5	1.76	0.08	32.0	>0.470	RGB J1756+553	17.3
J205528.2-002116		32.19	2.96	92.1	0.8	0.14	1.75	0.13	27.7	0.440	3FGL J2055.2-0019	18.0

model allows the source normalization to be optimized for each bin. In the second model the source spectrum is fixed to correspond to the null hypothesis, i.e. the source not being variable. For the first model, if the flux in a temporal bin was not significant ($TS < 9$) or if errors were larger than $\Delta F_i/F_i$, a 90 per cent confidence Bayesian upper limit was calculated with the *IntegralUpperLimit* module. Our variability index corresponds to that defined by *Fermi* in their 2FGL paper (Nolan et al. 2012),

$$TS_V = 2\sum_i \frac{\Delta F_i^2}{\Delta F_i^2 + f^2 F_c^2} V_i^2, \tag{3}$$

where ΔF_i is defined as the as the flux error, F_c the flux for the source if it was not variable, V_i^2 the difference in log-likelihoods for the null and alternative hypothesis, and f is a systematic correction factor determined by the *Fermi* team to be 0.02 in this calculation. For bins with low TS the variability was calculated using a similar statistic,

$$TS_{\mathrm{UL}} = 2\sum_i \frac{0.5(F_{UL} - F_i)^2}{0.5(F_{UL} - F_i)^2 + f^2 F_c^2} V_i^2. \tag{4}$$

The variability index is distributed as a χ^2 distribution where the degree of freedom corresponds to the number of bins, here 50. Thus, a total $TS_V > 63.17$ implies less than 10 per cent chance for the source to exhibit non-variability. For this analysis, a source with an index above this value is considered to be variable.

2.5 Source selection criteria

In choosing promising sources for follow-up, a set of criteria were placed on the sources to establish merit. A primary cut was imposed on the flux of each source, $F > 2.5 \times 10^{-10}$ cm^{-2} s^{-1}, to eliminate dim sources. It is also important that the sources have a hard photon index, $\gamma < 1.8$, and have low variability, $TS_V < 70$. From these cuts a list of 12 potentially promising sources was compiled (see Table 1). As a final means of selecting the most promising sources for observation, the hadronic and leptonic spectrum for each source was calculated and classified based on their detectability with IACTs. Sources which are detectable are put into two merit classes. Class I are likely detectable with current generation IACT detectors. Class II sources will likely take much longer for detection and are therefore better candidates for next-generation detectors like CTA. Sources are marked as belonging to one of these two classes in Table 1.

3 TEV SPECTRUM MODELLING

3.1 Leptonic scenario

With knowledge of the spectrum in the GeV regime, it is possible to predict the expected spectrum at TeV energies. For leptonic emission this can be done by assuming that the spectral index derived at GeV energies and extending the maximum energy while accounting for attenuation of γ-rays due to pair production on the EBL. In this scenario, the optical depth for EBL photons, $\tau_{\gamma\gamma}(E)$, is dependent on the redshift of the source. Thus, we can model the expected energy flux out to TeV energy,

$$EF_E = \mathcal{N}_{\mathrm{lep}} \cdot E^{-\gamma_{\mathrm{LAT}}+2} \cdot e^{-\tau_{\gamma\gamma}(E)}, \tag{5}$$

where $\mathcal{N}_{\mathrm{lep}}$ and γ_{LAT} are the flux normalization and spectral index in the LAT energy range as determined in our analysis. We have used data from Inoue et al. (2013) to calculate the attenuation of primary leptonic γ-rays.

3.2 UHECR-induced cascade scenario

Similar to primary γ-rays, cascades occur for UHECRs travelling through intergalactic space. The observed TeV spectrum, however, should be harder than in the leptonic case due to the injection of high-energy leptons from the Bethe–Heitler process. We adopt the analytic formula from Murase, Beacom & Takami (2012a) for such cascades (see also Berezinsky & Smirnov 1975). The approximate spectrum for the cascade emission is given by,

$$EG_E \propto \begin{cases} (E/E_{\mathrm{br}})^{1/2} & (E \le E_{\mathrm{br}}), \\ (E/E_{\mathrm{br}})^{2-\beta} & (E_{\mathrm{br}} \le E \le E_{\mathrm{cut}}), \end{cases} \tag{6}$$

where the normalization is set by $\int \mathrm{d}EG_E = 1$, with E_{cut}, the critical energy at which $\tau_{\gamma\gamma}(E) = 1$ due to the EBL absorption,for pair-production on the EBL, $E_{\mathrm{br}} \approx 4\varepsilon_{\mathrm{CMB}} E_e'^2/(3m_e^2)$ the energy below which the number of electrons remains constant, where $E_e' \approx (1+z)E_{\mathrm{cut}}/2$ and $\varepsilon_{\mathrm{CMB}} \approx 2.8 k_B T_{\mathrm{CMB},0}$, and the cascade photon index $\beta \approx 1.9$ (Murase et al. 2012a).

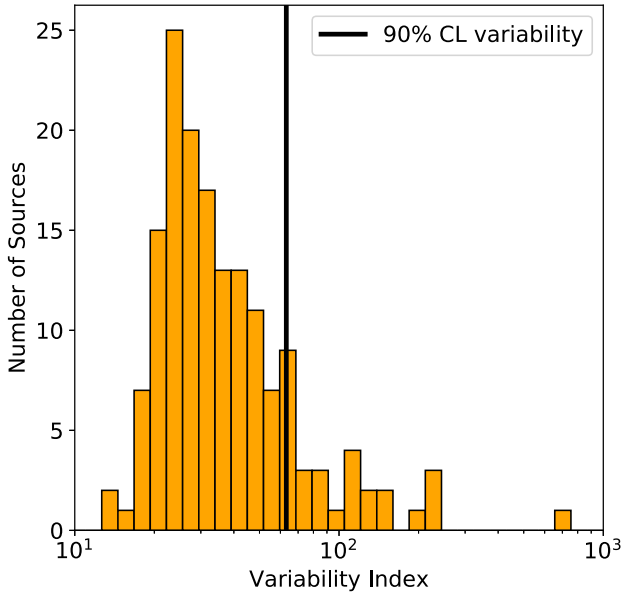

Figure 1. Distribution of the source variability index. The variability index for this analysis follows a χ^2 distribution with 50 degrees of freedom. Thus a source with a variability index in excess of 63.17 exhibits variability with 90 per cent confidence.

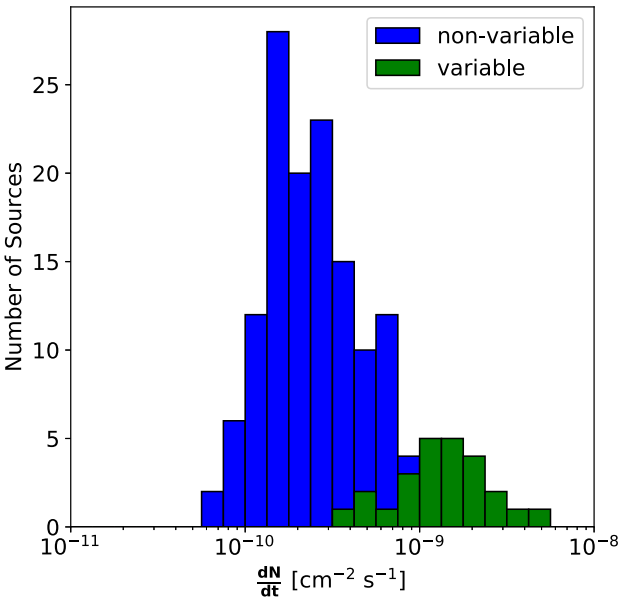

Figure 2. Distribution of fluxes over the 1–300 GeV band for non-variable and variable sources.

The optical depth to BH pair-production, $\tau_{\rm BH}$ for cosmic rays around 10^{19} eV, is given by the approximate expression,

$$\tau_{\rm BH} \approx \frac{d}{1000\ {\rm Mpc}}, \tag{7}$$

where d is the particle travel distance. Thus, the expected observed spectrum is given by,

$$EF_E = C_{\rm had} \cdot EG_E \frac{\min[1, \tau_{\rm BH}]}{\tau_{\gamma\gamma}(E)}(1 - \exp^{-\tau_{\gamma\gamma}(E)}), \tag{8}$$

where $C_{\rm had}$ is the normalization factor and this equation is implemented without a cutoff (because the cutoff shape is taken into account via $\tau_{\gamma\gamma}$). In addition, the low-energy spectrum is suppressed by IGMFs. The comparison with the point spread function of the *Fermi*-LAT (e.g. Neronov & Semikoz 2009; Murase et al. 2012a) suggests that the cascade emission is suppressed below ∼30 GeV for $B \sim 3 \times 10^{-17}$ G (see also equation 6 of Kotera, Allard & Lemoine 2011, and discussion).

In practice, our procedure provides the shape of the UHECR-induced cascade spectrum but does not encode the expected differential energy flux. Thus, we normalize our hadronic cascade spectrum using the normalization obtained through the *Fermi*data in the 10–100 GeV range.

4 RESULTS

4.1 Likelihood and variability results

In our analysis of 566 VHE γ-ray blazar candidates above $z \geq 0.2$ from the 2WHSP catalogue of HSP BL Lac objects, we detected 160 sources above $\approx 5\sigma$ ($TS \geq 25$). Our best-fitting spectral parameters and TS values are in agreement with previous analyses of these sources (Acero et al. 2015; Arsioli & Chang 2017).

Of the 160 γ-ray detected sources, 26 were found to exhibit variability with greater than 90 per cent confidence while 134 did not present variability (see Fig. 1). Based upon our criterion, the majority of our sources do not exhibit significant variability. Table 1 contains the results from the analysis for the most promising sources identified. The entire table with all sources from the analysis can be found in the Appendix.

Many of the sources in the 2WHSP catalogue do not have firm redshifts. While some sources have precise measurements, some have only lower limits, and others have measurements but uncertainties are still large. Where relevant, we separate data based on the nature of the redshift measurement.

The photon flux and luminosity distributions for non-variable and variable sources are plotted in Figs 2 and 3 respectively. For calculation of the luminosity we adopt the following cosmology, $\Omega_\Lambda = 0.7$, $\Omega_m = 0.3$, $\Omega_k = 0$, and $\rm H_0 = 70\,km\,s^{-1}\,Mpc^{-1}$.

These distributions clearly show that our non-variable sources are less bright than those which exhibit stronger variability. It is, however, less clear whether there is a correlation between variability and source luminosity. Our result could simply be due to the fact that variability is more easily seen for nearby sources.

In Fig. 4 the measured photon index is plotted against the calculated luminosity. For variable sources there appears to be a weak trend between these two parameters. A correlation test on the data reveals that the photon index is anticorrelated with source luminosity at $\approx 2\sigma$ confidence. On the other hand, there is no apparent correlation for non-variable data. Characteristic error bars are depicted in Fig. 4 for variable and non-variable sources which corresponds to the average error for each class. Additionally plotted was variability index against the photon index in Fig. 5 to see if there was a correlation. If one considers the data set as a whole, there is no apparent correlation. Even further consideration of the strongest sources implies there is no correlation between hardness and variability. In Fig. 5 we make this distinction by considering sources with a $TS < 450$ as being sources with less confident variability. Note that a non-variable source with $TS = 450$ with a variability index calculated over 50 time intervals will have a test statistic for a per bin in the light-curve, corresponding to $\approx 3\sigma$.

Indeed, the true nature of the variability for each source should be considered. It is more than likely that many of the sources from this

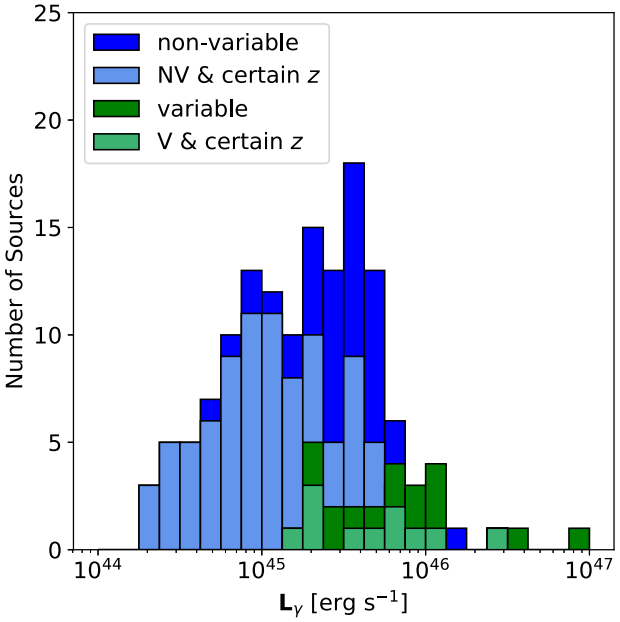

Figure 3. Distribution of luminosity over the 1–300 GeV band for non-variable (blue) and variable (green) sources. The light colour corresponds to sources with confident redshift measurements. Variable and non-variable sources are represented by 'V' and 'NV', respectively.

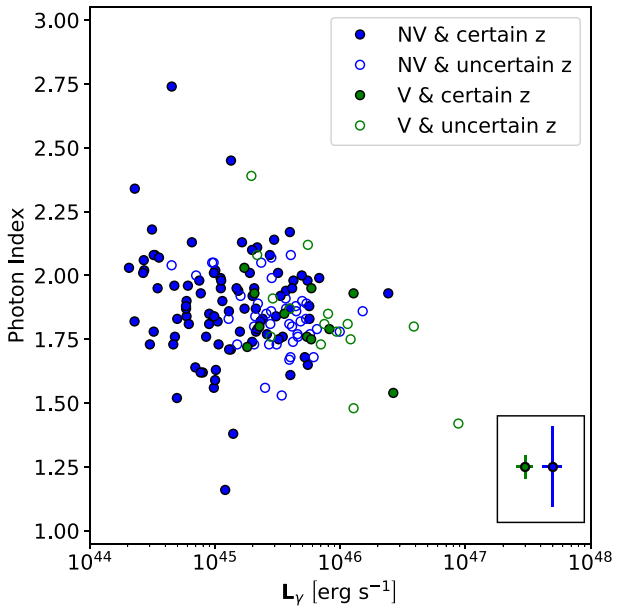

Figure 4. Source luminosities against the photon index. The open circles correspond to sources of uncertain redshift. The legend at the lower right corner shows the characteristic error bars for sources of confident redshift.

analysis do exhibit some variability, to which our analysis is not yet sensitive. In Fig. 6, where we plot the source luminosity as a function of redshift, it is interesting to note that the variable and non-variable sources can be roughly partitioned by plotting the luminosity for a given energy flux over a range of redshifts. In Fig. 7 we plot the variability as a function of test statistic. There is, unsurprisingly, a strong apparent correlation between the two.

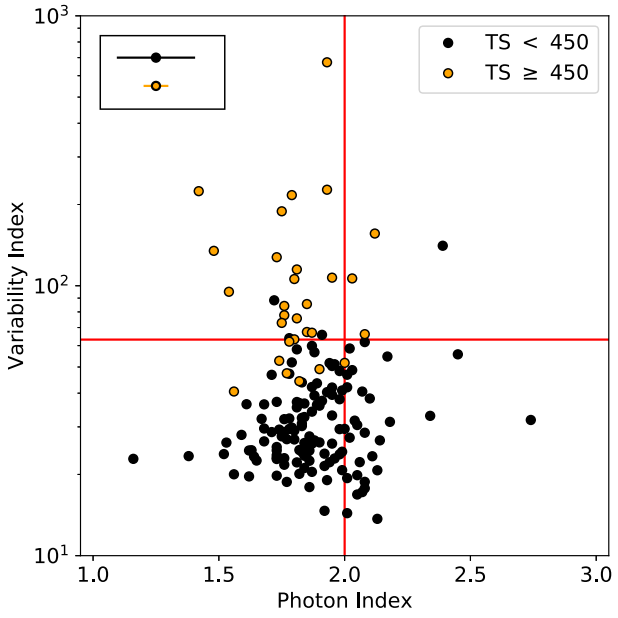

Figure 5. Plot of the variability versus the photon index. Note that we have artificially split the data by choosing $TS \geq 450$. This corresponds to an average TS per temporal bin of 3. The red vertical line indicates a photon index $n = 2$ and the red horizontal line indicates the 90 per cent confidence limit on source variability. Characteristic error bars for both classes are given in the legend of the upper left of the figure.

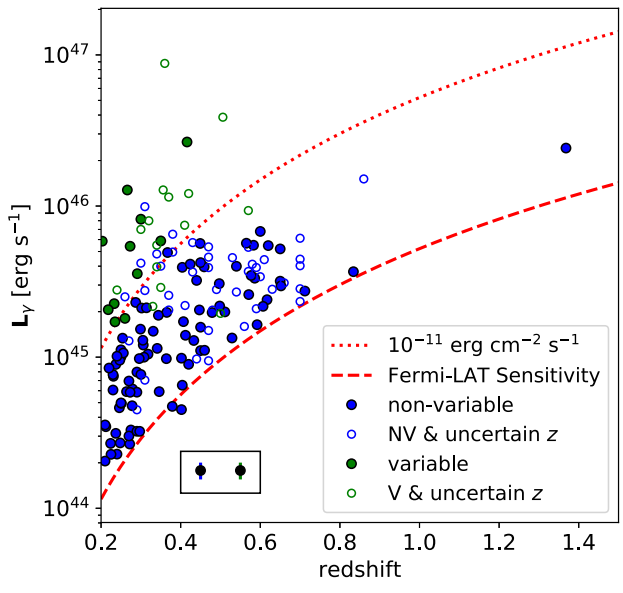

Figure 6. Luminosity is plotted against redshift for the sources where open circles correspond to uncertain redshift. The thick dashed line corresponds to the 8 yr, 5σ *Fermi*-LAT detection threshold. Characteristic error bars are given in the legend on the lower left of the figure.

4.2 Promising sources

From the results of the likelihood and variability analyses, significant sources were discriminated based on their variability, redshift, and brightness, to establish the best candidates with the potential for a hadronic signature to be observed by IACTs, including the Cherenkov Telescope Array (CTA) (Cherenkov Telescope Array Consortium 2019), Major Atmospheric Gamma Imaging Cherenkov

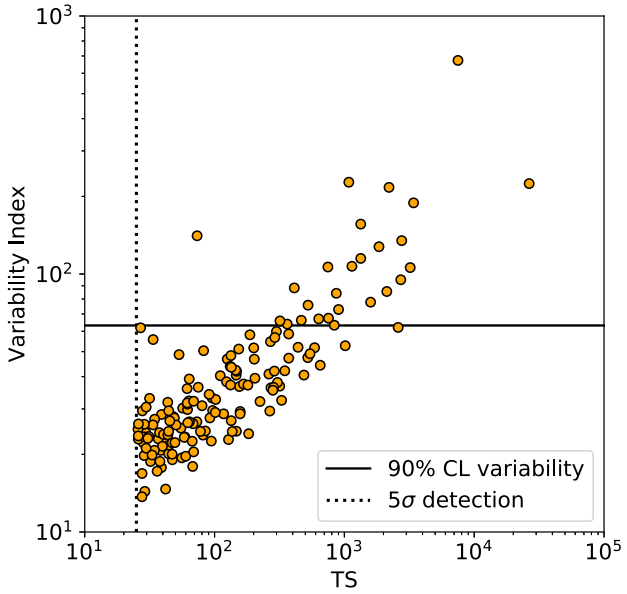

Figure 7. Source variability index plotted against its *TS* value. The solid black line indicates the 90 per cent confidence limit on source variability and the vertical dashed line the $TS \geq 25$, $\approx 5\sigma$, detection threshold. Note that there are no sources below a $TS = 25$ as these did not meet the detection threshold.

Telescopes (MAGIC) (Aleksić et al. 2016a), High Energy Stereoscopic System (H.E.S.S) (H. E. S. S. Collaboration 2017), and Very Energetic Radiation Imaging Telescope Array System (VERITAS) (Holder et al. 2008).

We have identified four sources as Class I, based on the criterion that they may be detectable with current IACTs. We present them in turn, below.

4.2.1 1ES 1028+511

Source 2WHSP J103118.4+505335, 3FGL J1031.2+5053, also known with the name 1ES 1028+511, shown in Fig. 8, is a promising candidate for observation by CTA and potentially MAGIC and VERITAS, based on our *Fermi* analysis. This source has been observed by VERITAS for 24.1 h, yielding an upper limit of 7.7×10^{-12} erg^{-1} cm^{-2} s^{-1} (Archambault et al. 2016). Interestingly, for this source the VERITAS upper limit constrains the hadronic model for the level of flux predicted with the best-fitting *Fermi* index. Thus additional observations of this source may be very sensitive to or otherwise very constraining of the hadronic model. Additionally, with $\log \nu_S = 17.0$ it is interesting as a possible extreme-HSP source.

4.2.2 RBS 1366

With a detection significance of $\approx 12\sigma$, a very low variability index, and a firm redshift determination (Ahn et al. 2012), 2WHSP J141756.5+254324, 3FGL J1417.8+2540, also known as RBS 1366, is also a promising candidate for detecting with TeV instruments. The large uncertainties in the *Fermi*-LAT analysis however mean that we cannot conclusively determine whether the source will be detectable. Under optimistic assumptions (upper 1σ uncertainty range) it is a good candidate for observation by CTA or VERITAS and also possibly by MAGIC. A differential upper limit of 1.7×10^{-11} erg^{-1}cm^{-2}s^{-1} at 327 GeV was calculated for this source by VERITAS based on 10 h of observations, but is not sufficient to constrain the hadronic origin model (Archambault et al. 2016). With synchrotron peak frequency at $\log \nu_S = 17.4$, this source is possibly an extreme-HSP, and thus interesting to study at VHE even if it is purely leptonic, for the purpose of furthering our knowledge of this, small and extreme source population. It was also flagged as a TeV blazar candidate by the analysis of Costamante (2020).

4.2.3 RBS 621

The blazar RBS 621 (3FGL J0506.9-5435, 2WHSP J050657.7-543503), with *Fermi*-LAT detection significance of around 23.0 σ and low variability $TS_V = 40.6$, is another source promising for TeV detection and for the detection of the UHECR hadronic signature. The redshift is uncertain with a lower limit of $z > 0.26$. To the best of our knowledge this source has not yet been observed with H.E.S.S., but it is our most promising source for detection with a 50 h exposure if the true redshift is close to the lower limit and certainly promising for observations with CTA.

4.2.4 RBS 1457

The blazar RBS 1457 (3FGL J1503.7-1540,2WHSP J150340.6-154113) is also one of the sources most promising for TeV detection and for detection of the hadronic cascade signature in our sample, with *Fermi*-LAT detection significance of around 21.0 σ and low variability $TS_V = 52$. There is only a lower limit on the redshift of this source, $z > 0.38$, but if the true redshift is not much higher than the lower limit, this source, at declination $\delta = -15.4^\circ$ is possibly detectable with H.E.S.S. and it is certainly a promising source for CTA South.

4.2.5 Other promising sources

We have found a number of additional promising sources, which we categorized as Class II because they likely require an instrument with sensitivity comparable to that of CTA for detection. We show their γ-ray spectra in Fig. A1, in the Appendix. The source 2WHSP J143657.7+563924, or RBS 1409, or RX J1436.9+5639, is one of these sources. An upper limit was obtained based on a 13 h observation of the source with VERITAS (Aliu et al. 2012). A redshift of $z = 0.15$ has been quoted based on the redshift of a galaxy cluster within the same region of the sky (Bauer et al. 2000). However, the optical spectrum of the galaxy is featureless (Aliu et al. 2012). We thus assumed a redshift value equal to the lower limit quoted by the more recent work of Chang et al. (2017) in this work. The Class II sample additionally contains Ton 116, which at redshift $z = 1.065$, if detected with CTA could give unambigious evidence of the hadronic cascade. The additional notable candidates include 3FGL J1124.9+4932-RBS 981, at redshift $z > 0.57$, and RGB 1756+553 at redshift $z > 0.57$, both suitable with observations with North sky instruments, as well as 3FGL J0118.9-145 at redshift $z > 0.530$ and 1ES 0602-482 in the Southern sky.

Two sources from Table 1, 3FGL J2055.2-0019 and 3FGL J1012.7+4229, are not included as promising sources for observation even though they met the initial selection criteria. It was clear that current and future IACTs lack the sensitivity to detect the hadronic component of these sources in a reasonable observation period.

5 DISCUSSION AND CONCLUSIONS

We have analysed the *Fermi* data for 566 HSP blazars from the 2WHSP catalogue. By discriminating significant sources with

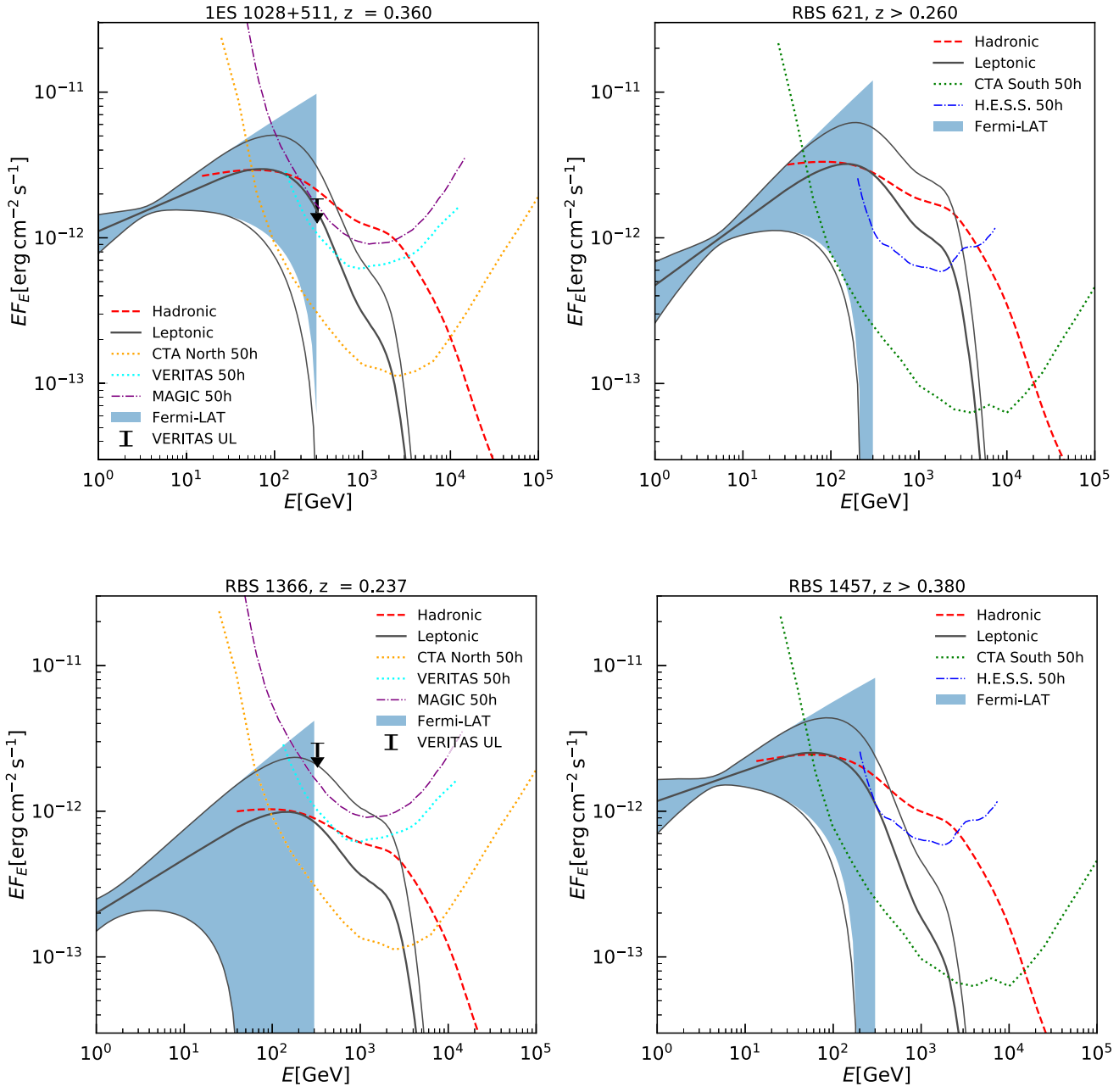

Figure 8. Modelled leptonic spectrum (thick black) with 1σ confidence interval (grey) and the UHECR-induced cascade spectrum (solid red) of our promising sources based upon analysis of the *Fermi*-LAT data, shaded blue, in the GeV regime. Also plotted are the sensitivity curves for 50 h observations with detectors that can see the source. Sensitivities for CTA , North (yellow) and South (green), from Hassan et al. (2017), MAGIC (purple) (Aleksić et al. 2016b), H.E.S.S. (blue), (Holler et al. 2015) and VERITAS (cyan). Upper limits were calculated for the sources 1ES 1218+511 and RBS 1366 from observations with VERITAS (Archambault et al. 2016).

Fermi-LAT data in the GeV band based on the hardness of spectrum, limited variability, and detectability with current and future IACTs, we have compiled a list of the most promising sources for TeV follow-up observations. By extending the GeV spectrum to greater than TeV energies and modelling the expected γ-ray spectrum under the assumption of both leptonic and hadronic origins, we have shown that if the sources are UHECR accelerators, and magnetic fields in the intergalactic medium are low, it will be possible to distinguish between a leptonic or UHECR-induced cascade scenario in these sources using CTA.

The motivation for our analysis has been twofold. First, to identify blazars whose γ-ray spectra can be used, if a detection with IACTs is achieved, to constrain the extragalactic magnetic field by considering their combined GeV–TeV spectra (e.g. Murase et al. 2008; Neronov & Semikoz 2009; Neronov & Vovk 2010; Tavecchio et al. 2010; Dermer et al. 2011; Dolag et al. 2011; Taylor, Vovk & Neronov 2011). Secondly, to identify blazars which could exhibit a hard spectrum in the TeV energy range, which could be the signature of UHECR acceleration and emission from these sources, as has been previously discussed for a handful of extreme HSPs (e.g.

Essey & Kusenko 2010; Essey et al. 2011; Murase et al. 2012b; Aharonian et al. 2013; Takami et al. 2013; Oikonomou et al. 2014; Tavecchio 2014; Dzhatdoev et al. 2017; Cherenkov Telescope Array Consortium 2019; Khalikov & Dzhatdoev 2019; Tavecchio et al. 2019). Recently the MAGIC Collaboration announced the detection of 2WHSP J073326.7+515354 (Acciari et al. 2019) at $\gtrsim$1 TeV energies. The source does not form part of our sample, since it lies at $z = 0.06$ and doesn't satisfy the $z \geq 0.2$ cut. However, the search for TeV emission from this source demonstrates the interest for detectable HSP and extreme HSP sources, as well as some of the open questions on blazar emission which can be addressed with similar IACT observations.

In our analysis the majority of sources were found to lack any significant variability. While blazars as a class are well known for their variability, this result cannot exclude the presence of variability, since these are relatively faint sources, and any intrinsic variability may be below the experimental sensitivity of *Fermi*. As expected in this statistically limited regime, the sources that do exhibit significant variability in our analysis are the brightest sources in terms of flux. Therefore, our results are not conclusive in regards to the question whether some of the sources examined could be powered by secondary γ-rays from UHECR primaries. In the latter case, there should be no detectable variability in the γ-ray energy range since UHECRs get delayed by magnetic fields. Given that the bright sources in our sample are all consistent with being variable, our results are consistent with all sources being intrinsically variable and thus powered by leptonic emission mechanisms, giving no conclusive support to the UHECR-induced cascade scenario.

It is important to emphasize again how our variability results differ from those which accompany the 4FGL catalogue. The most important difference is the energy range over which the variability index was calculated. In our analysis we used a higher energy threshold of 1 GeV than the 100 MeV threshold of the 4FGL, which is better suited for the hard spectrum sources of interest in our analysis and might allow us, to better isolate the the hadronic component which, if present, should be dominant above $\sim$10–100 GeV as demonstrated in previous sections. The present analysis was conducted using data from the *Fermi* launch to late 2016. An updated analysis should reach the same conclusion, but surely with improved uncertainties ($\approx$10 per cent with 2 more years of data).

While this work was being finalized, the 3HSP catalogue, which is the largest and most complete HSP catalogue available to date, became available (Chang et al. 2019). With respect to the 2WHSP it contains 395 additional HSP blazars. In the future, our analysis could be extended to include these additional sources.

ACKNOWLEDGEMENTS

This work was initiated in 2016 for the honors thesis 'BLAZARS AS A SOURCE FOR ULTRA-HIGH-ENERGY COSMIC RAYS? A SEARCH FOR THE ELUSIVE HADRONIC SIGNATURE' at the Schreyer Honors College of Penn State University in 2018. We thank Gordana Tešić for fruitful input during the early stages of this work. We also thank Akira Okumura for useful comments on sensitivity curves. The work of KM is supported by the Alfred P. Sloan Foundation, NSF Grant No. AST-1908689, and KAKENHI No. 20H01901.

DATA AVAILABILITY

The data underlying this article are available in the article.

REFERENCES

Abeysekara A. U. et al., 2015, ApJ, 815, L22
Acciari V. A. et al., 2019, MNRAS, 490, 2284
Acero F. et al., 2015, ApJS, 218, 23
Aharonian F. A., 2000, New Astron., 5, 377
Aharonian F. A., Coppi P. S., Volk H. J., 1994, ApJ, 423, L5
Aharonian F., Essey W., Kusenko A., Prosekin A., 2013, Phys. Rev. D, 87, 063002
Ahn C. P. et al., 2012, ApJS, 203, 21
Ahnen M. L. et al., 2016, A&A, 595, A98
Aleksić J. et al., 2016a, Astropart. Phys., 72, 61
Aleksić J. et al., 2016b, Astropart. Phys., 72, 76
Aliu E. et al., 2012, ApJ, 759, 102
Alves Batista R. et al., 2019, Front. Astron. Space Sci., 6, 23
Anchordoqui L. A., 2019, Phys. Rep., 801, 1
Archambault S. et al., 2016, AJ, 151, 142
Archambault S. et al., 2017, ApJ, 835, 288
Arsioli B., Chang Y. L., 2017, A&A, 598, A134
Arsioli B., Barres de Almeida U., Prandini E., Fraga B., Foffano L., 2018, MNRAS, 480, 2165
Atwood W. B. et al., 2009, ApJ, 697, 1071
Bauer F. E., Condon J. J., Thuan T. X., Broderick J. J., 2000, ApJS, 129, 547
Berezinsky V. S., Smirnov A. Yu., 1975, Ap&SS, 32, 461
Biteau J. et al., 2020, Nat. Astron., 4, 124
Chang Y. L., Arsioli B., Giommi P., Padovani P., 2017, A&A, 598, A17
Chang Y.-L., Arsioli B., Giommi P., Padovani P., Brandt C. H., 2019, A&A, 632, A77
Cherenkov Telescope Array Consortium, 2019, Science with the Cherenkov Telescope Array. WSP, Singapore
Costamante L., 2020, MNRAS, 491, 2771
Costamante L. et al., 2001, A&A, 371, 512
Costamante L., Bonnoli G., Tavecchio F., Ghisellini G., Tagliaferri G., Khangulyan D., 2018, MNRAS, 477, 4257
Dermer C. D., Razzaque S., 2010, ApJ, 724, 1366
Dermer C. D., Cavadini M., Razzaque S., Finke J. D., Chiang J., Lott B., 2011, ApJ, 733, L21
Dolag K., Kachelriess M., Ostapchenko S., Tomàs R., 2011, ApJ, 727, L4
Dzhatdoev T. A., Khalikov E. V., Kircheva A. P., Lyukshin A. A., 2017, A&A, 603, A59
Elyiv A., Neronov A., Semikoz D. V., 2009, Phys. Rev. D, 80, 023010
Essey W., Kusenko A., 2010, Astropart. Phys., 33, 81
Essey W., Kalashev O., Kusenko A., Beacom J. F., 2011, ApJ, 731, 51
Fermi-LAT Collaboration, 2010, ApJ, 716, 30
Ginzburg V. L., Syrovatskii S. I., 1964, The Origin of Cosmic Rays. Pergamon, New York
Gould R. J., Rephaeli Y., 1978, ApJ, 225, 318
Gould R., Schréder G., 1966, Phys. Rev. Lett., 16, 252
H. E. S. S. Collaboration, 2014, A&A, 562, A145
H. E. S. S. Collaboration, 2017, A&A, 600, A89
Hassan T. et al., 2017, Astropart. Phys., 93, 76
Hillas A. M., 1984, ARA&A, 22, 425
Holder J. et al., 2008, in Aharonian F. A., Hofmann W., Rieger F., eds, AIP Conf. Proc. Vol. 1085, Proceedings of the 4th International Meeting on High Energy Gamma-Ray Astronomy. Am. Inst. Phys., New York, p. 657
Holler M. et al., 2015, Proc. Sci., International Cosmic Ray Conference (ICRC2015). SISSA, Trieste, PoS#847
Inoue Y., Inoue S., Kobayashi M. A. R., Makiya R., Niino Y., Totani T., 2013, ApJ, 768, 197
Katarzynski K., Ghisellini G., Tavecchio F., Gracia J., Maraschi L., 2006, MNRAS, 368, L52
Khalikov E. V., Dzhatdoev T. A., 2019, preprint (arXiv:1912.10570)
Kotera K., Olinto A. V., 2011, ARA&A, 49, 119
Kotera K., Allard D., Lemoine M., 2011, A&A, 527, A54
Maraschi L., Ghisellini G., Celotti A., 1992, ApJ, 397, L5
Mollerach S., Roulet E., 2018, Prog. Part. Nucl. Phys., 98, 85

Mücke A., Protheroe R. J., 2001, Astropart. Phys., 15, 121
Murase K., Fukugita M., 2019, Phys. Rev. D, 99, 063012
Murase K., Takahashi K., Inoue S., Ichiki K., Nagataki S., 2008, ApJ, 686, L67
Murase K., Mészáros P., Zhang B., 2009, Phys. Rev., D79, 103001
Murase K., Beacom J. F., Takami H., 2012a, J. Cosmol. Astropart. Phys., 8, 030
Murase K., Dermer C. D., Takami H., Migliori G., 2012b, ApJ, 749, 63
Neronov A., Semikoz D., 2009, Phys. Rev., D80, 123012
Neronov A., Vovk I., 2010, Science, 328, 73
Nolan P. L. et al., 2012, ApJS, 199, 31
Oikonomou F., Murase K., Kotera K., 2014, A&A, 568, A110
Padovani P., Giommi P., 1995, ApJ, 444, 567
Prosekin A., Essey W., Kusenko A., Aharonian F., 2012, ApJ, 757, 183
Rodrigues X., Fedynitch A., Gao S., Boncioli D., Winter W., 2018, ApJ, 854, 54
Sikora M., Begelman M. C., Rees M. J., 1994, ApJ, 421, 153
Stecker F. W., de Jager O. C., Salamon M. H., 1992, ApJ, 390, L49
Takahashi K., Murase K., Ichiki K., Inoue S., Nagataki S., 2008, ApJ, 687, L5
Takami H., Murase K., Dermer C. D., 2013, ApJ, 771, L32
Takami H., Murase K., Dermer C. D., 2016, ApJ, 817, 59
Tavecchio F., 2014, MNRAS, 438, 3255
Tavecchio F., Ghisellini G., Foschini L., Bonnoli G., Ghirlanda G., Coppi P., 2010, MNRAS, 406, L70
Tavecchio F., Romano P., Landoni M., Vercellone S., 2019, MNRAS, 483, 1802
Taylor A. M., Vovk I., Neronov A., 2011, A&A, 529, A144
The Fermi-LAT collaboration, 2019, ApJS, 247, 33
Urry C. M., Padovani P., 1995, PASP, 107, 803
Wood M., Caputo R., Charles E., Di Mauro M., Magill J., Perkins J. S., Fermi-LAT Collaboration, 2017, Proc. Sci., International Cosmic Ray Conference (ICRC2017), SISSA, Trieste, PoS#824

APPENDIX A:

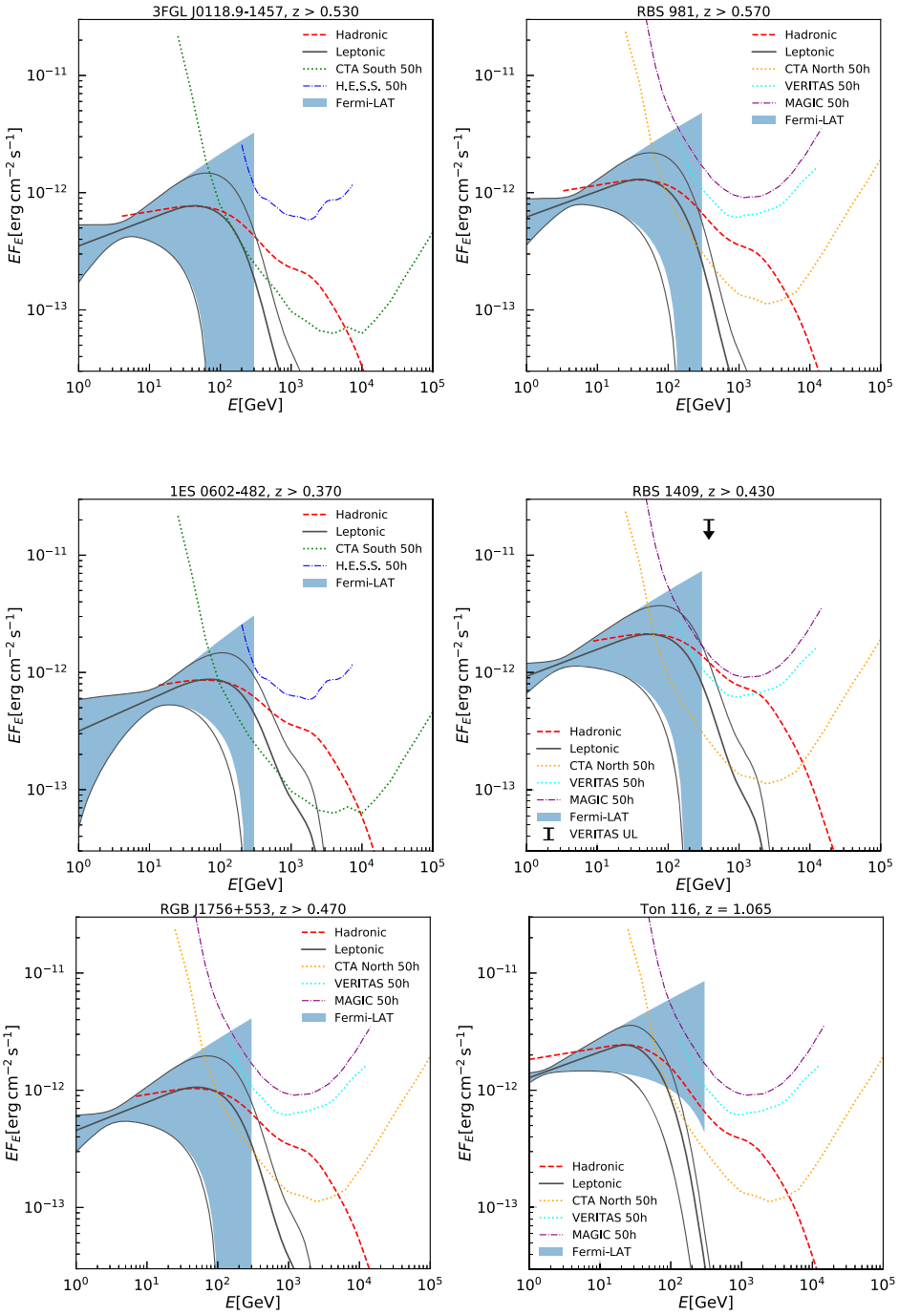

Figure A1. Modelled leptonic spectrum (thick black) with 1σ confidence interval (grey) and the UHECR-induced cascade spectrum (solid red) of our promising sources based upon analysis of the *Fermi*-LAT data, shaded blue, in the GeV regime. Also plotted are the sensitivity curves for 50 h observations with detectors that can see the source. Sensitivities for CTA, North (yellow) and South (green), from Hassan et al. (2017), MAGIC (purple) (Aleksić et al. 2016b), H.E.S.S. (blue), (Holler et al. 2015) and VERITAS (cyan). Upper limits were calculated for the source RBS 1409 from observations with VERITAS (Aliu et al. 2012).

Table A1. Results from the analysis of 2WHSP sources. Included is the name from the 2WHSP catalogue, the luminosity from 1 to 300 GeV, L_{44}, in units of 10^{44} erg s^{-1}, the 1–300 GeV photon flux, $(\mathrm{d}N/\mathrm{d}t)_{-10}$, in units of 10^{-10} cm^{-2} s^{-1}, the test statistic from the likelihood fit , TS, the normalization and its error scaled by 10^{-11} cm^{-2} s^{-1} GeV^{-1}, N_{-11} and σ_N, the photon index γ and its error σ_γ, the variability index TS_V (> 63.17 is a variable source), the source redshift z, a statement on the uncertainty of the redshift (T means redshift is uncertain), and alternative identifier, and the logarithm of the synchrotron peak frequency, $\log \nu_{\mathrm{S,pk}}$ in units of log Hz.

2WHSP Name	L_{44}	$(\frac{\mathrm{d}N}{\mathrm{d}t})_{-10}$	TS	N_{-11}	σ_N	γ	σ_γ	TS_V	z	U_z	Other Name	$\log \nu_{\mathrm{S,pk}}$
J002200.9+000657	12.03	0.66	40.37	0.5	0.37	1.16	0.27	22.84	0.306		–	16.3
J020412.9-333339	24.01	1.17	29.49	1.31	0.41	1.83	0.21	24.26	0.617		1BIGB J020412.9-3333	17.9
J023536.6-293843	31.01	1.02	25.84	1.12	0.44	1.73	0.24	23.57	>0.660		–	15.8
J030103.7+344100	2.28	2.43	31.57	2.5	0.57	2.34	0.23	32.96	0.240		1BIGB J030103.7+3441	15.7
J030433.9-005403	19.92	1.82	41.97	2.05	0.58	1.92	0.2	14.66	0.511		1BIGB J030433.9-0054	15.4
J031423.8+061955	54.73	3.53	81.43	3.94	0.75	1.98	0.15	23.74	0.620	T	1BIGB J031423.8+0619	16.3
J035856.1-305447	31.82	1.94	55.99	2.16	0.46	2.01	0.18	19.38	0.650	T	1BIGB J035856.1-3054	16.9
J050335.3-111506	36.91	2.35	68.98	2.64	0.62	1.87	0.16	20.44	>0.570		1BIGB J050335.3-1115	16.9
J060714.2-251859	3.3	1.77	39.03	1.95	0.46	2.08	0.2	28.54	0.275		1BIGB J060714.2-2518	17.5
J062149.6-341148	13.39	2.56	33.64	2.51	0.57	2.45	0.25	55.71	0.529		1BIGB J062149.6-3411	17.7
J062337.7-525756	9.73	1.65	27.64	1.82	0.51	2.05	0.25	16.85	>0.440		–	15.2
J062626.2-171045	40.25	2.33	37.95	2.56	0.65	2.08	0.22	18.77	>0.700		1BIGB J062626.2-1710	16.6
J073152.6+280432	2.71	1.65	34.55	1.83	0.47	2.02	0.22	27.36	0.248		1BIGB J073152.6+2804	17.0
J074929.5+745143	21.69	1.86	59.17	2.04	0.4	2.11	0.18	23.35	0.607	T	–	16.1
J083724.5+145819	4.77	1.29	36.82	1.44	0.46	1.76	0.2	22.97	0.278		1BIGB J083724.5+1458	16.7
J090953.2+310602	2.66	1.29	29.04	1.43	0.43	2.01	0.25	14.37	0.272		1BIGB J090953.2+3106	17.0
J095214.6+393615	23.35	1.28	29.72	1.42	0.41	2.05	0.25	30.48	>0.700		1FGL J0952.2+3926	16.5
J095507.9+355100	36.78	1.07	28.26	1.2	0.39	1.94	0.25	22.19	0.834		1BIGB J095507.9+3551	17.5
J100612.1+644010	15.96	1.19	39.66	1.33	0.36	1.92	0.19	21.49	>0.560		–	15.4
J101706.6+520247	4.72	0.96	25.88	1.07	0.33	1.96	0.24	22.91	0.379		–	15.8
J103346.3+370824	20.53	2.79	95.99	3.12	0.54	1.95	0.14	33.06	0.447		–	17.1
J104857.6+500945	4.5	2.12	43.59	1.82	0.44	2.74	0.32	31.82	0.402		1BIGB J104857.6+5009	17.4
J110357.1+261117	27.38	1.53	38.98	1.68	0.42	2.08	0.22	17.77	0.712	T	–	17.9
J113444.6-172900	25.94	1.33	32.13	1.49	0.55	1.77	0.23	18.76	0.571		1BIGB J113444.6-1729	16.9
J121158.6+224233	11.05	1.6	37.65	1.78	0.46	1.99	0.21	24.27	0.450		1BIGB J121158.6+2242	17.6
J122307.2+110038	241.85	2.04	47.3	2.29	0.52	1.93	0.17	19.05	1.368	T	–	16.1
J124141.4+344029	28.34	1.39	34.42	1.56	0.42	1.99	0.22	20.74	>0.700		1BIGB J124141.4+3440	16.6
J125847.9-044744	33.29	2.22	40.44	2.48	0.69	1.92	0.2	23.87	0.586	T	1BIGB J125847.9-0447	16.9
J130145.6+405623	29.61	2.25	73.12	2.45	0.44	2.14	0.17	26.74	0.652		1BIGB J130145.6+4056	15.9
J131234.6-185900	28.13	2.09	36.1	2.3	0.58	2.07	0.23	17.2	>0.630		–	16.0
J133102.8+565541	3.01	0.82	28.69	0.9	0.33	1.73	0.21	19.78	0.270		–	17.6
J135328.0+560056	6.52	1.53	38.42	1.67	0.4	2.13	0.22	20.72	0.404		1BIGB J135328.0+5600	16.3
J142421.1+370552	3.23	1.54	26.92	1.69	0.54	2.08	0.29	61.85	0.290		–	16.3
J152913.5+381216	20.92	1.15	29.7	1.29	0.38	1.84	0.2	21.12	>0.590		1BIGB J152913.5+3812	15.7
J160218.0+305108	9.47	1.36	33.01	1.51	0.4	2.05	0.22	19.87	>0.470		1BIGB J160218.0+3051	15.6
J164220.2+221143	16.4	1.55	27.61	1.69	0.51	2.13	0.26	13.69	0.592		1BIGB J164220.2+2211	16.5
J164419.9+454644	2.27	1.16	44.21	1.3	0.38	1.82	0.2	20.1	0.225		1BIGB J164419.9+4546	16.3
J165249.9+402309	7.05	2.46	44.36	2.74	0.63	2.0	0.18	29.49	>0.310		–	15.5
J174702.5+493800	11.11	1.39	33.52	1.56	0.44	1.95	0.22	26.01	0.460	T	1BIGB J174702.5+4938	17.0
J184822.4+653656	9.77	0.89	47.14	0.94	0.34	1.56	0.18	20.02	0.364		1BIGB J184822.4+6536	17.7
J194455.0-214318	74.63	9.18	524.94	10.28	0.91	1.81	0.07	75.71	>0.410		–	16.0
J213852.6-205347	7.97	1.45	60.01	1.56	0.45	1.62	0.16	19.66	0.290		2FGL J2139.1-2054	17.0
J224910.6-130002	19.48	4.01	73.38	4.02	0.66	2.39	0.2	140.67	>0.500		1BIGB J224910.6-1300	17.5
J225147.5-320611	4.63	1.57	55.04	1.73	0.5	1.73	0.19	25.27	0.246		1BIGB J225147.5-3206	18.0
J002200.0-514023	10.03	6.0	372.36	19.59	2.18	2.02	0.08	58.56	0.250		3FGL J0022.1-5141	15.7
J003020.4-164712	8.95	3.93	187.25	1.72	0.22	1.81	0.11	58.11	0.237		3FGL J0030.2-1646	15.6
J003334.3-192132	387.12	28.57	3214.1	47.87	2.04	1.8	0.03	105.89	>0.506		3FGL J0033.6-1921	15.7
J004334.0-044300	20.48	1.71	45.21	0.48	0.12	1.8	0.2	26.95	>0.480		3FGL J0043.5-0444	16.7
J004348.6-111606	5.91	2.44	68.34	0.73	0.14	1.9	0.15	26.28	0.264		3FGL J0043.7-1117	15.7
J005116.6-624203	70.01	15.13	1847.48	10.64	0.54	1.73	0.04	127.56	>0.300		3FGL J0051.2-6241	15.9
J011130.1+053626	5.91	1.16	28.78	0.85	0.27	1.84	0.22	26.15	0.346		3FGL J0111.5+0535	16.5
J011904.6-145858	45.54	2.82	134.42	1.82	0.29	1.77	0.12	27.01	>0.530		3FGL J0118.9-1457	16.1
J012338.2-231058	39.29	5.71	299.7	9.61	1.14	1.87	0.08	59.86	0.404		3FGL J0123.7-2312	17.3
J015646.0-474417	4.49	1.99	61.6	1.5	0.3	2.04	0.19	31.64	>0.290		3FGL J0156.9-4742	16.6
J020838.1+352312	10.47	2.42	84.95	0.69	0.12	1.82	0.15	24.63	0.318		3FGL J0208.6+3522	16.3
J021252.7+224452	39.57	7.42	269.67	33.49	4.02	2.17	0.08	54.67	0.459		3FGL J0213.0+2245	15.2
J021650.8-663642	21.68	7.57	465.79	16.52	1.4	2.08	0.08	66.16	>0.330		3FGL J0217.0-6635	15.5
J022716.4+020159	42.23	5.95	266.31	16.94	2.12	1.98	0.08	29.43	0.450		3FGL J0227.2+0201	17.6
J023734.0-360328	21.97	3.19	134.68	2.79	0.43	1.89	0.12	43.5	>0.411		3FGL J0237.5-3603	16.0

Table A1 – *continued*

2WHSP Name	L_{44}	$(\frac{dN}{dt})_{-10}$	TS	N_{-11}	σ_N	γ	σ_γ	TS_V	z	U_z	Other Name	$\log \nu_{S,pk}$
J023832.3-311656	22.59	10.19	835.93	14.51	1.1	1.8	0.05	63.3	0.233		3FGL J0238.4-3117	16.3
J024440.1-581954	18.05	5.29	411.39	1.82	0.17	1.72	0.08	88.32	0.260		3FGL J0244.8-5818	16.8
J030326.3-240710	127.67	55.28	7499.57	340.74	12.35	1.93	0.02	672.76	0.266		3FGL J0303.4-2407	15.7
J030416.3-283217	61.21	1.56	62.22	0.45	0.1	1.68	0.16	26.51	>0.700		3FGL J0304.3-2836	17.7
J032523.5-563544	67.9	4.9	262.21	31.81	4.85	1.99	0.07	40.94	0.600		3FGL J0325.2-5634	16.5
J032540.9-164615	35.67	10.75	754.22	10.94	0.8	1.85	0.06	67.4	0.291		3FGL J0325.6-1648	15.6
J033812.4-244350	4.95	0.96	43.72	0.05	0.02	1.52	0.19	23.79	0.251		3FGL J0338.1-2443	17.1
J041652.3+010522	23.01	6.7	317.69	2.76	0.28	1.82	0.08	36.76	0.287		3FGL J0416.8+0104	16.5
J050534.6+041553	41.26	6.32	204.81	3.17	0.38	1.95	0.11	39.44	0.424		3FGL J0505.5+0416	15.7
J050657.7-543503	25.07	5.05	488.15	2.21	0.21	1.56	0.07	40.57	>0.260		3FGL J0506.9-5435	16.2
J050756.0+673723	265.31	17.08	2720.35	5.27	0.23	1.54	0.03	95.0	0.416	T	3FGL J0508.0+6736	17.9
J053628.9-334301	55.09	19.18	1336.69	379.34	33.18	2.12	0.03	156.11	>0.340		3FGL J0536.4-3347	16.0
J054357.1-553207	54.18	15.6	1592.31	15.17	0.83	1.76	0.04	77.78	0.273		3FGL J0543.9-5531	16.7
J055806.4-383830	21.14	6.14	347.52	8.0	0.84	1.87	0.08	42.16	0.302		3FGL J0558.1-3838	16.7
J060408.5-481725	20.5	2.69	132.76	0.26	0.05	1.73	0.11	37.13	>0.370		3FGL J0604.1-4817	16.2
J064443.6-285115	28.03	2.53	67.3	4.2	0.96	1.86	0.12	22.47	>0.490		3FGL J0644.6-2853	16.1
J065046.3+250258	58.54	32.21	3411.1	25.7	0.96	1.75	0.03	188.73	0.203	T	3FGL J0650.7+2503	16.8
J074405.2+743357	21.21	4.58	372.66	7.65	0.87	1.78	0.07	47.18	0.314		3FGL J0744.3+7434	16.7
J080457.7-062425	36.6	4.97	166.99	2.57	0.34	1.91	0.11	37.46	>0.430		3FGL J0805.0-0622	16.9
J080625.9+593106	7.68	2.51	110.66	1.73	0.28	1.93	0.13	40.34	0.300	T	3FGL J0806.6+5933	15.3
J081627.1-131152	114.61	18.07	1336.78	17.85	1.01	1.81	0.04	114.91	>0.370		3FGL J0816.4-1311	16.4
J082706.1-070844	9.54	4.04	155.31	7.63	1.25	1.84	0.09	36.62	0.247	T	3FGL J0827.2-0711	16.3
J090534.9+135805	48.19	9.5	651.36	13.0	1.07	1.82	0.06	44.29	>0.340		3FGL J0905.5+1358	15.1
J091037.0+332924	58.77	14.17	1143.74	15.9	0.91	1.95	0.05	107.14	0.350	T	3FGL J0910.5+3329	15.0
J091230.5+155527	3.47	2.62	82.34	0.1	0.03	1.95	0.11	50.43	0.212		3FGL J0912.7+1556	16.9
J091714.5-034314	9.99	1.44	48.02	0.62	0.17	1.59	0.17	28.02	0.308		3FGL J0917.3-0344	16.6
J092542.7+595815	44.5	1.67	67.85	0.43	0.08	1.86	0.15	17.95	>0.700		3FGL J0925.6+5959	15.5
J094022.3+614825	3.56	3.47	146.74	25.57	4.66	2.07	0.09	40.55	0.210		3FGL J0941.0+6151	16.2
J094620.2+010450	34.71	1.71	44.65	0.33	0.08	1.76	0.19	21.72	0.577		3FGL J0946.2+0103	17.9
J095805.8-031739	34.06	0.88	25.94	0.18	0.06	1.53	0.22	26.24	>0.600		3FGL J0958.3-0318	16.4
J101244.2+422957	19.77	2.78	157.36	1.01	0.14	1.74	0.11	29.31	0.365		3FGL J1012.7+4229	16.8
J102339.7+300056	12.89	1.55	49.01	0.51	0.12	1.86	0.19	27.66	0.433		3FGL J1023.7+3000	15.8
J103118.4+505335	41.89	9.22	1014.96	7.26	0.48	1.74	0.05	52.72	>0.360		3FGL J1031.2+5053	17.0
J104149.0+390118	2.05	1.85	53.25	2.71	0.59	2.03	0.17	48.69	0.210		3FGL J1041.8+3901	16.5
J104651.4-253544	4.98	2.04	56.87	1.29	0.28	1.83	0.16	30.21	0.250		3FGL J1046.9-2531	18.0
J105125.3+394324	30.66	2.58	101.98	1.19	0.19	1.84	0.14	32.63	0.497		3FGL J1051.4+3941	16.8
J110124.7+410847	41.2	2.18	101.33	0.79	0.14	1.8	0.14	29.06	>0.580		3FGL J1101.5+4106	15.7
J110747.9+150209	11.18	6.18	305.15	14.09	1.6	1.98	0.08	37.98	0.250	T	3FGL J1107.8+1502	15.6
J111224.5+175120	8.97	1.14	25.7	0.07	0.03	1.85	0.22	25.04	0.420		3FGL J1112.6+1749	16.9
J111939.4-304720	13.95	0.62	28.6	0.1	0.04	1.38	0.23	23.38	0.412		3FGL J1119.7-3046	17.1
J112453.8+493409	93.35	4.89	362.65	2.91	0.29	1.78	0.08	63.95	>0.570		3FGL J1124.9+4932	16.5
J112551.9-074220	6.16	1.86	47.16	1.78	0.47	1.81	0.16	22.16	0.279		3FGL J1125.8-0745	15.7
J114930.3+243925	9.84	1.35	31.19	1.28	0.43	1.84	0.19	23.45	0.402		3FGL J1149.5+2443	17.1
J115034.6+415439	79.88	19.26	2122.31	29.82	1.46	1.85	0.04	85.54	>0.320		3FGL J1150.5+4155	15.6
J115404.5-001009	13.36	3.99	202.3	1.47	0.2	1.71	0.1	46.77	0.254		3FGL J1154.2-0010	16.6
J115853.2+081942	5.86	1.84	50.53	1.12	0.25	1.87	0.19	25.99	0.290		3FGL J1158.9+0818	16.1
J120412.1+114555	9.78	3.91	125.3	3.26	0.47	2.01	0.13	46.81	0.296		3FGL J1204.0+1144	16.6
J121945.7-031422	15.32	5.15	200.41	9.2	1.3	1.94	0.09	51.71	0.299		3FGL J1219.7-0314	16.0
J122424.1+243623	20.61	14.18	1081.89	16.98	1.02	1.93	0.05	226.87	0.218		3FGL J1224.5+2436	16.1
J122644.2+063853	55.02	2.04	94.42	0.37	0.07	1.65	0.14	22.51	0.583		3FGL J1226.8+0638	15.8
J123123.8+142124	10.65	3.27	128.07	4.74	0.87	1.73	0.09	22.81	0.256		3FGL J1231.8+1421	15.4
J123738.9+625841	3.23	0.8	27.79	0.42	0.13	1.78	0.22	29.47	0.297		3FGL J1237.9+6258	16.0
J124312.7+362743	99.06	21.98	2594.81	33.1	1.52	1.78	0.03	62.08	>1.065		3FGL J1243.1+3627	16.2
J131532.5+113330	44.19	2.44	63.8	1.83	0.36	1.88	0.15	39.18	>0.610		3FGL J1315.4+1130	16.7
J132301.0+043951	2.69	2.22	49.54	0.76	0.16	2.06	0.19	22.21	0.224		3FGL J1322.9+0435	16.8
J132358.3+140558	53.68	5.75	271.93	13.23	1.65	1.89	0.08	36.22	>0.470		3FGL J1323.9+1405	15.4
J134029.8+441004	39.93	1.62	74.83	0.7	0.16	1.61	0.14	36.4	0.540		3FGL J1340.6+4412	17.3
J140450.8+040202	25.64	4.39	183.09	7.71	1.14	1.85	0.09	24.03	>0.370		3FGL J1404.8+0401	15.7
J140659.1+164206	26.99	1.46	44.26	0.33	0.08	1.73	0.18	24.55	>0.540		3FGL J1406.6+1644	17.0
J141756.5+254324	10.14	2.86	147.3	7.2	1.65	1.63	0.08	24.58	0.237		3FGL J1417.8+2540	17.4
J141826.2-023333	127.76	28.2	2765.72	57.51	2.33	1.48	nan	134.68	>0.356		3FGL J1418.4-0233	15.5
J141900.3+773229	12.81	4.34	328.47	5.14	0.53	1.83	0.07	32.38	>0.270		3FGL J1418.9+7731	16.0
J143657.7+563924	57.3	5.79	522.39	8.28	0.8	1.77	0.06	47.4	>0.430		3FGL J1436.8+5639	16.9

Table A1 – *continued*

2WHSP Name	L_{44}	$(\frac{dN}{dt})_{-10}$	TS	N_{-11}	σ_N	γ	σ_γ	TS_V	z	U_z	Other Name	$\log \nu_{S,pk}$
J143917.3+393242	18.93	5.28	289.04	3.68	0.37	2.01	0.1	42.05	0.344		3FGL J1439.2+3931	15.9
J144037.7-384654	40.0	5.42	285.18	1.5	0.16	1.68	0.08	36.35	>0.350		3FGL J1440.4-3845	17.2
J144506.1-032612	27.6	6.55	281.39	10.13	1.24	1.81	0.07	35.43	>0.310		3FGL J1445.0-0328	17.4
J145127.7+635419	52.03	1.61	96.65	1.03	0.2	1.68	0.13	29.58	0.650		3FGL J1451.2+6355	17.0
J150101.7+223806	17.13	11.95	746.59	25.58	1.81	2.03	0.06	106.44	0.235		3FGL J1500.9+2238	15.1
J150340.6-154113	65.09	9.18	439.69	5.04	0.42	1.79	0.07	52.0	>0.380		3FGL J1503.7-1540	17.6
J150716.3+172102	56.74	3.44	131.85	1.5	0.21	1.83	0.11	43.84	0.565		3FGL J1507.4+1725	15.7
J150842.5+270908	6.95	1.54	58.39	0.48	0.11	1.64	0.16	23.28	0.270		3FGL J1508.6+2709	17.8
J153311.2+185429	12.93	2.56	117.52	1.86	0.35	1.71	0.11	28.7	0.305		3FGL J1533.2+1852	17.2
J153500.7+532036	39.18	1.48	68.96	1.78	0.44	1.67	0.12	32.12	>0.590		3FGL J1534.4+5323	17.2
J154604.2+081913	28.91	6.47	318.97	2.55	0.25	1.91	0.08	65.78	>0.350		3FGL J1546.0+0818	15.1
J154712.1-280221	53.33	3.12	80.1	0.93	0.16	1.83	0.14	30.87	>0.570		3FGL J1547.1-2801	15.8
J155424.1+201125	5.85	2.15	64.0	6.92	1.95	1.88	0.11	26.73	0.273		3FGL J1554.4+2010	17.4
J155543.0+111123	878.53	140.08	26507.02	468.11	7.41	1.42	nan	224.09	>0.443		3FGL J1555.7+1111	15.6
J160620.8+563016	15.78	1.48	63.57	0.88	0.2	1.78	0.16	32.23	0.450		3FGL J1606.1+5630	16.0
J162625.8+351341	21.79	1.64	61.92	0.48	0.1	1.79	0.16	29.82	0.498		3FGL J1626.1+3512	16.0
J170238.5+311542	39.15	3.54	180.58	0.51	0.07	1.81	0.09	37.09	>0.470		3FGL J1702.6+3116	15.4
J175615.9+552218	45.88	3.68	223.86	3.85	0.5	1.76	0.08	32.04	>0.470		3FGL J1756.3+5523	17.3
J175713.0+703337	17.18	2.45	90.8	0.31	0.06	1.87	0.13	34.16	0.407		3FGL J1756.9+7032	17.3
J183849.0+480234	81.84	20.04	2206.35	20.22	0.93	1.79	0.04	216.67	0.300	T	3FGL J1838.8+4802	15.8
J201428.6-004721	7.47	4.92	133.66	3.21	0.44	1.98	0.12	48.3	0.231	T	3FGL J2014.3-0047	15.2
J201624.0-090333	49.24	11.68	589.46	27.26	2.22	2.0	0.06	51.79	0.367	T	3FGL J2016.4-0905	15.0
J203649.3-332830	7.66	2.31	77.87	0.12	0.03	1.62	0.12	24.53	0.230		3FGL J2036.6-3325	16.3
J205528.2-002116	32.19	2.96	92.1	0.8	0.14	1.75	0.13	27.67	0.440		3FGL J2055.2-0019	18.0
J213103.1-274656	49.59	8.82	543.82	4.85	0.38	1.9	0.07	49.09	>0.380		3FGL J2130.8-2745	16.1
J213135.3-091523	56.54	6.51	291.27	14.19	1.76	1.88	0.07	56.71	0.449		3FGL J2131.5-0915	16.4
J213151.4-251557	151.09	3.49	136.81	5.01	0.82	1.86	0.11	24.51	>0.860		3FGL J2131.8-2516	16.9
J214552.1+071927	3.13	2.75	61.8	89.18	37.36	2.18	0.09	31.31	0.237		3FGL J2145.7+0717	17.5
J214636.9-134359	120.94	12.42	901.51	6.88	0.46	1.75	0.05	72.84	>0.420		3FGL J2146.6-1344	15.7
J215015.4-141049	8.47	3.92	157.35	2.51	0.36	1.76	0.1	28.71	0.220		3FGL J2150.2-1411	17.8
J215305.2-004229	11.43	2.66	61.44	2.04	0.47	1.9	0.16	35.95	0.341		3FGL J2152.9-0045	18.0
J222129.2-522527	39.59	8.71	634.52	16.4	1.36	1.87	0.06	66.99	>0.340		3FGL J2221.6-5225	15.8
J225818.9-552536	19.73	2.97	123.74	19.87	4.03	2.1	0.1	38.22	0.479		3FGL J2258.3-5526	15.7
J230722.0-120517	15.01	1.13	30.63	0.57	0.19	1.73	0.21	23.05	>0.470		3FGL J2307.4-1208	16.5
J232444.5-404049	27.82	10.72	866.67	7.26	0.51	1.76	0.06	84.18	>0.240		3FGL J2324.7-4040	15.5
J235034.3-300603	6.06	3.93	153.56	8.61	1.3	1.96	0.11	51.19	0.230		3FGL J2350.4-3004	15.7
J235612.1+403643	14.84	4.02	147.69	1.19	0.16	1.95	0.11	41.97	0.331		3FGL J2356.0+4037	16.3

This paper has been typeset from a TEX/LATEX file prepared by the author.